Onset of convective instabilities in under-ice melt ponds

Sílvia C. Hirata[*]
Laboratoire de Mécanique de Lille, Bld Paul Langevin 59655 Villeneuve d'Ascq Cédex, France

Benoît Goyeau[†] and Dominique Gobin[‡]
Laboratoire EM2C, UPR CNRS 288, Ecole Centrale Paris, Grande Voie des Vignes - 92295 Châtenay-Malabry, France
(Received 24 May 2011; revised manuscript received 26 March 2012; published 8 June 2012)

The onset of double-diffusive natural convection in under-ice melt ponds is investigated through a linear stability analysis. The three-layer configuration is composed by a fluid layer (melt pond) overlying a saturated porous medium (ice matrix), which in turn overlies another fluid layer (under-ice melt pond). Water density inversion is taken into account by adopting a density profile with a quadratic temperature dependence and a linear concentration dependence. We show that the key parameter affecting stability is the depth of the ice matrix, while the depths of the upper and lower fluid layers play a marginal role. A Hopf bifurcation is observed in the whole range of parameters studied, and the size of the convection cells depends on ice permeability. The influence of the external temperature gradient is investigated by means of the definition of an extra thermal parameter accounting for the relative position of the density maximum. It is shown that convection is favored by larger temperature gradients, which occur during Arctic summer.

DOI: 10.1103/PhysRevE.85.066306 PACS number(s): 44.25.+f, 44.30.+v, 47.20.−k, 47.56.+r

I. INTRODUCTION

The Arctic sea cover is an important component of the global climate system. While a great amount of information is available on large-scale processes [1], little attention has been paid to smaller scale processes occurring on the evolution of the Arctic ice pack. In this context, we focus our attention on a process associated with ice ablation during the Arctic summer. When the air temperature is above 0 °C, the surface of sea ice begins to melt, forming a pond of fresh water or *melt pond*. Meltwater can percolate into the ice matrix, leading to a strong reduction in the surface salinity [2], and gets discharged under the ice. In this situation, a layer of fresh meltwater at a temperature of approximately 0 °C is retained between a layer of ice and a much colder (≈−1.6 °C) and denser layer of salty sea water, forming a so-called *under-ice melt pond*. A schematic diagram of the system is presented in Fig. 1. Due to the fact that the density of pure water below 4 °C is a decreasing function of temperature, this system is convectively unstable with respect to the temperature gradient, and therefore double-diffusive convection can occur. The evolution of under-ice melt ponds was first described by Martin and Kauffman [3]. They showed, through laboratory experiments, that in the initial convective process the supercooled water rises to the overlying ice layer leading to the formation of thin vertical ice crystals. In a second stage, they observed a lateral growth of the vertical crystals at the fresh-salty water interface, forming an ice-sheet which is usually called a *false bottom*. Thereafter, the horizontal ice-sheet slowly migrates upward due to bottom ablation, while it increases in thickness. Notz *et al.* [4] and Alexandrov and Nizovtseva [5] presented mathematical models to describe the evolution of false bottoms, which were treated as mushy layer regions. The formation of false bottoms is believed to be the only process by which ice can be formed during summer [6]. It is also important to emphasize that, as shown by the field experiment Surface Heat Budget of the Arctic Ocean (SHEBA) [7], the water in under-ice melt ponds has the highest percental amount of snow meltwater among all meltwater reservoirs. Taking into consideration that under-ice melt ponds might be a widespread phenomenon in the Arctic [8], this may probably cause a significant transfer of pollutants from the atmosphere into the ice pack, which could lead to an accumulation of pollutants at the biologically important ice underside [9].

Few studies in the literature had been dedicated to the analysis of the physical mechanisms influencing the onset of convection in under-ice melt ponds. The understanding of the base mechanism in a simplified system is a fundamental step in the comprehension of the problem. Therefore, the aim of this paper is to model the first stage in the evolution of under-ice melt ponds, i.e., the onset of double-diffusive instabilities in the three-layer system composed by the melt pond, the ice matrix, and the under-ice melt pond. In order to account for the water density inversion at 4 °C, we choose a density profile with quadratic temperature dependence and linear concentration dependence. Through a linear stability analysis, we obtain the conditions for the onset of convective movement in the ponds, which is the first step for the formation of false bottoms. The ice matrix is modeled as a saturated porous medium and we do not consider phase change. The influence of the salty sea water layer is taken into account by imposing appropriate boundary conditions at the lower interface. Bogorodskii and Nagurnyi [10] presented a model for the same three-layer system; however, they have assumed the water to be isoconcentrational, and hence the salinity gradients were neglected. The results of the pure thermal problem without density inversion were obtained using symmetry arguments, and indicate that the decrease in ice thickness favors the development of instabilities. Carr [11] studied the double-diffusive problem in a single fluid layer including water density inversion, and results show that the

[*]silvia.hirata@univ-lille1.fr
[†]benoit.goyeau@ecp.fr
[‡]dominique.gobin@ecp.fr

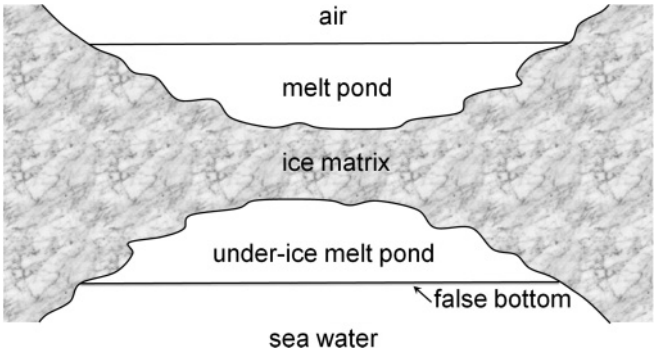

FIG. 1. Schematic diagram of an under-ice melt pond.

onset of convection can be either stationary or oscillatory. Differently from the previously mentioned papers, we consider the problem of double-diffusive natural convection in the three-layer system, which is modeled using a one-domain formulation [12–15]. The paper is organized as follows. After presenting the governing equations of the one-domain approach in Sec. II, a linear stability analysis is carried out in Sec. III. In Sec. IV, our numerical results are validated with the case of a single fluid layer [11]. Then, the influence of the depth ratio, external temperature difference, and permeability of the porous medium on the stability characteristics of the system is investigated. The implications on the modeling of under-ice melt ponds are discussed and, in Sec. V, we present some concluding remarks.

II. MATHEMATICAL MODELING

The system under consideration consists of an infinite horizontal porous layer of thickness d_m^* sandwiched between two fluid layers (cf. Fig. 2). The thickness of the lower and upper fluid layers are denoted d_b^* and d_u^*, respectively, while $d^* = d_b^* + d_m^* + d_u^*$ represents the total thickness of the system. The saturated porous medium is assumed to be homogeneous and isotropic, and phase change is not taken into account. The upper and lower external walls are impermeable and kept at different temperatures ($T_u^* > T_b^*$) and salt concentrations ($S_u^* < S_b^*$). In this configuration, the system is gravitationally unstable since density increases with temperature and the top water is warmer. On the other hand, the bottom water has a higher salt concentration. Therefore, we are in the presence of two competing effects: a destabilizing temperature field and a stabilizing salinity field.

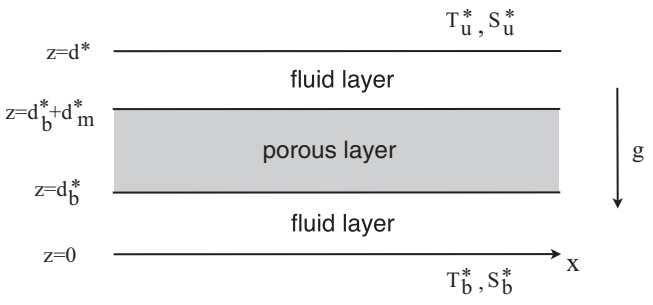

FIG. 2. Geometric configuration of the problem.

In order to take the water density inversion into account, the density profile is assumed to be of the form

$$\rho(T^*, S^*) = \rho_0[1 - \gamma_T(T^* - T_0^*)^2 - \beta_S(S^* - S_0^*)], \quad (1)$$

where γ_T and β_S are the thermal and the solute expansion coefficients, respectively. We are aware that the local solute concentration influences the temperature T_0^* and the value of the density maximum ρ_0 [16]. However, for simplicity reasons, we shall take the approximative value for pure water: $T_0^* = 4\,^\circ$C. S_0^* is some constant reference value.

In the one-domain approach, the porous medium is considered as a pseudofluid and a unique set of conservation equations is written for the entire domain. Hence the explicit formulation of the boundary conditions at the fluid-porous interfaces is avoided, considerably simplifying the numerical resolution of the system. Details concerning the application of the one-domain formulation to fluid-porous systems can be found in previous works [12–15] and, for the sake of conciseness, shall not be repeated here. The dimensionless conservation equations are obtained using the following scales: d^* for length, d^{*2}/ν for time, ν/d^* for velocity, and $(\rho_0\nu^2)/d^{*2}$ for pressure, where ν is the kinematic viscosity of the fluid. The temperature and the concentration fields are scaled by $\Delta T = T_u^* - T_b^*$ and $\Delta S = S_u^* - S_b^*$, respectively.

The set of one-domain dimensionless conservation equations, valid both in the fluid and in the porous regions, can be written as

$$\nabla \cdot \mathbf{u} = 0, \quad (2)$$

$$\frac{\partial}{\partial t}\left(\frac{\mathbf{u}}{\phi}\right) + \frac{1}{\phi}\left(\mathbf{u}\cdot\nabla\frac{\mathbf{u}}{\phi}\right) = \nabla\cdot\left(\frac{1}{\phi}\nabla\mathbf{u} - P\mathbf{I}\right) - \frac{1}{\mathrm{Da}}\mathbf{u} + (\mathrm{Gr}_\mathrm{T}^* T^2 + \mathrm{Gr}_\mathrm{S} S)\mathbf{e}_z, \quad (3)$$

$$\frac{\partial T}{\partial t} + \mathbf{u}\cdot\nabla T = \frac{1}{\mathrm{Pr_f}}\nabla\cdot\left(\frac{\alpha_T}{\alpha_{Tf}}\nabla T\right), \quad (4)$$

$$\phi\frac{\partial S}{\partial t} + \mathbf{u}\cdot\nabla S = \frac{1}{\mathrm{Sc_f}}\nabla\cdot(\phi\nabla S), \quad (5)$$

where $\mathbf{I}$ represents the identity matrix. $\mathrm{Gr}_\mathrm{T}^* = (g\gamma_T\Delta T^2 d^{*3})/\nu^2$ and $\mathrm{Gr_S} = (g\beta_S\Delta S d^{*3})/\nu^2$ are respectively the thermal and solutal Grashof numbers based on the total depth of the channel d^*. It is important to remark that the momentum conservation equation (3) obtained using a density profile with quadratic temperature dependence leads to the introduction of a modified thermal Grashof number Gr_T^*. Note that the form of the density law (1) implies $\gamma_T > 0$ and $\beta_S < 0$. Therefore, we have $\mathrm{Gr}_\mathrm{T}^* > 0$ and $\mathrm{Gr_S} > 0$ (as $\Delta S < 0$).

In the present problem, one has to define an extra parameter which accounts for the difference between the lower wall temperature and the reference temperature: $\xi = (T_b^* - T_0^*)/\Delta T$. This point will be further discussed in Sec. IV B4. $\mathrm{Pr_f} = \nu/\alpha_{Tf}$ and $\mathrm{Sc_f} = \nu/D_f$ are the fluid Prandtl and Schmidt numbers, respectively. In the solute transport Eq. (5), due to absence of mass diffusion in the solid phase, the effective solute diffusion coefficient in the absence of dispersion effects has been taken such that $D_{\mathrm{eff}} = \phi D_f$, where ϕ represents the porosity. In the momentum conservation Eq. (3), the Darcy number represents the dimensionless permeability ($\mathrm{Da} = K/d^{*2}$) and the reduced

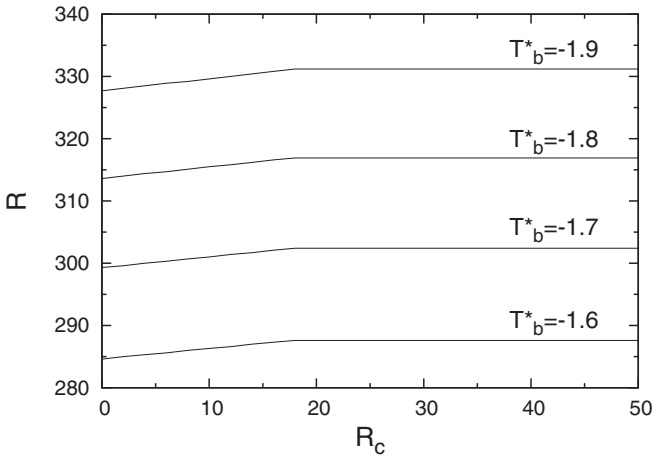

FIG. 3. Linear stability curves for a single fluid layer. As in Ref. [11], $R = g\gamma_T \Delta T^2 d^{*3}/(\nu\alpha_{Tf})$ represents the fluid thermal Rayleigh number, and $R_c = g\beta_S \Delta S d^{*3}/(\nu D_f)$ is the fluid solutal Rayleigh number.

dynamic viscosity in the Brinkman term has been taken such that $\mu_{\text{eff}}/\mu_f = 1/\phi$ [17]. Note that Da $\to \infty$ in the fluid layer. Finally, α_T in Eq. (4) is the thermal diffusivity ($\alpha_T = \alpha_{Tm}$ in the porous medium and $\alpha_T = \alpha_{Tf}$ in the fluid).

The dimensionless boundary conditions at the external walls are

$$\begin{aligned} \mathbf{u}(1) = 0, \quad \theta(1) = \frac{T_u^* - T_0^*}{\Delta T}, \quad S(1) = \frac{S_u^* - S_0^*}{\Delta S}, \\ \mathbf{u}(0) = 0, \quad \theta(0) = \frac{T_b^* - T_0^*}{\Delta T}, \quad S(0) = \frac{S_b^* - S_0^*}{\Delta S}. \end{aligned} \tag{6}$$

In the one-domain formulation, the effective properties (ϕ, Da, and α_T) are Heaviside functions and therefore their differentiation must be considered in the meaning of distributions, as detailed in Ref. [12].

III. LINEAR STABILITY ANALYSIS

The perturbation equations are obtained in the usual way. We assume that the percolation velocity of the melt water through the ice matrix, during the formation of the under-ice melt pond, is such that the diffusive profile of temperature and salt concentration can be established throughout the system. Thus the base state is quiescent. For conciseness,

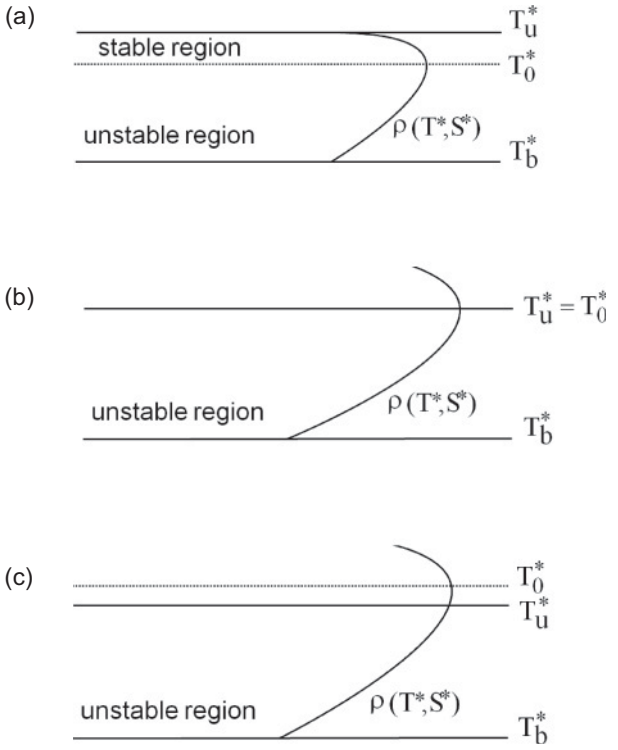

FIG. 4. (a) $\xi > -1$: the temperature domain encompasses the temperature of the density maximum (penetrative convection). The present study concerns cases (b) $\xi = -1$ and (c) $\xi < -1$: the temperature of the density maximum lies outside the temperature domain. In these situations, the reference temperature difference ΔT is the "effective range" for the onset of convection.

the temperature and concentration base solutions are provided in the Appendixes. According to the normal mode expansion, the vertical velocity component, the temperature, and the concentration are decomposed under the form

$$(w', T', S') = [W(z), \theta(z), \mathcal{S}(z)] e^{i\kappa x + \sigma t}, \tag{7}$$

where $W(z)$, $\theta(z)$, and $\mathcal{S}(z)$ are the amplitudes of the perturbed variables, κ is the dimensionless wave number, and $\sigma = \sigma_r + i\sigma_i$ is a complex: σ_r represents the temporal growth rate and σ_i is the oscillation frequency.

Neglecting the nonlinear terms, the linearized system takes the form

$$\begin{aligned} &\left(\frac{d(1/\phi)}{dz}\frac{dW}{dz} + \frac{1}{\phi}\frac{d^2W}{dz^2} - \frac{1}{\phi}\kappa^2 W\right)\sigma + \frac{1}{\phi}\left(\frac{d^4W}{dz^4} + \kappa^4 W\right) \\ &- \left(-2\frac{d(1/\phi)}{dz}\frac{d^3W}{dz^3} - \frac{d(1/\mathrm{Da})}{dz}\frac{dW}{dz} + \frac{1}{\mathrm{Da}}\frac{d^2W}{dz^2} - \frac{d^2(1/\phi)}{dz^2}\frac{d^2W}{dz^2}\right) \\ &- \kappa^2\left(\frac{2}{\phi}\frac{d^2W}{dz^2} - \frac{1}{\mathrm{Da}}W + 2\frac{d(1/\phi)}{dz}\frac{dW}{dz}\right) + \kappa^2[\mathrm{Gr}_\mathrm{T}^*\theta(2\,\overline{T}) + \mathrm{Gr}_\mathrm{S}\mathcal{S}] = 0, \end{aligned} \tag{8}$$

$$\mathrm{Pr}_\mathrm{f}\left(\sigma\theta + \frac{d\overline{T}}{dz}W\right) = \frac{\alpha_T}{\alpha_{Tf}}\left(-\kappa^2\theta + \frac{d^2\theta}{dz^2}\right) + \frac{1}{\alpha_{Tf}}\frac{d\alpha_T}{dz}\frac{d\theta}{dz}, \tag{9}$$

$$\mathrm{Sc}_\mathrm{f}\phi\left(\sigma\mathcal{S} + \frac{d\overline{S}}{dz}W\right) = \phi\left(-\kappa^2\mathcal{S} + \frac{d^2\mathcal{S}}{dz^2}\right) + \frac{d\phi}{dz}\frac{d\mathcal{S}}{dz}, \tag{10}$$

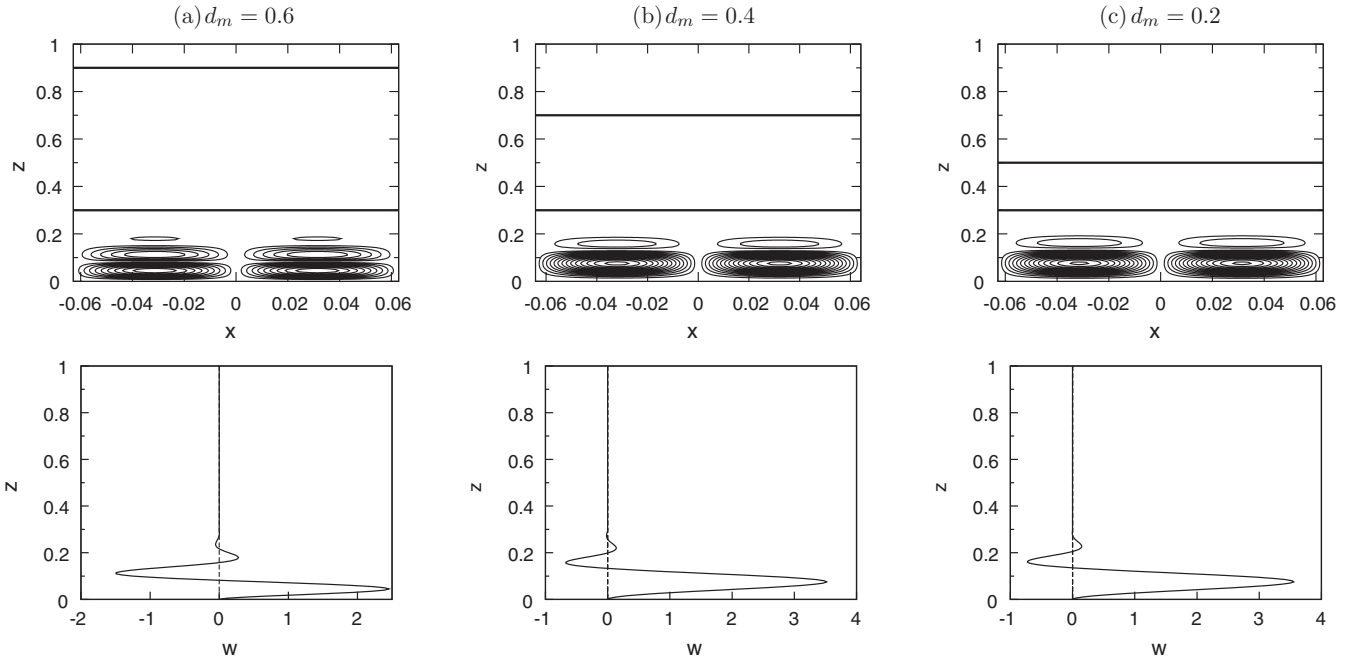

FIG. 5. Streamline patterns ($\Psi_{max} = \pm 0.07$, $\Delta\Psi = 0.01$) and vertical velocity profiles at the onset of convection for $Ra_S = 900$, $\xi = -1$, $Da = 10^{-8}$, $d_b = 0.3$, and different values of d_m. The thick horizontal lines represent the fluid-porous interfaces.

with boundary conditions

$$\theta(1) = 0, \quad \mathcal{S}(1) = 0, \quad W(1) = 0, \quad \frac{dW(1)}{dz} = 0,$$
$$\theta(0) = 0, \quad \mathcal{S}(0) = 0, \quad W(0) = 0, \quad \frac{dW(0)}{dz} = 0. \tag{11}$$

The system of equations (8)–(11) is solved using the generalized integral transform technique (GITT) [18]. After applying the integral transformation, the resulting eigenvalue problem is written under the form $\mathbf{A} - \sigma\mathbf{B} = 0$, and solved for the eigenvalues $\sigma^{(N)}$, $N = 1,2,\ldots$. Matrices $\mathbf{A}$ and $\mathbf{B}$ are given in the Appendixes. The reader is referred to Refs. [13,14] for details concerning the application of the GITT to such fluid-porous configurations. To produce the marginal stability curves, we fixed κ and Gr_S, and found Gr_T^* such that $\sigma_r = 0$. We then tracked through κ and Gr_S to produce the curves. The converged results were obtained using a precision of ± 0.05 in Gr_T^*.

IV. RESULTS AND DISCUSSION

A. Validation: Single fluid layer

Results of the GITT applied to the one-domain formulation were already validated within the framework of a linear Boussinesq approximation for the pure thermal case [13] and the double-diffusive case [15]. These works concerned the stability of a fluid-porous system without density inversion. In order to validate the analysis and the numerical code for a density profile with a quadratic temperature dependence, we first compare our results to those obtained by Carr [11] for a single fluid layer ($Da \to \infty$, $\phi = 1$). As in Ref. [11], we fix $Pr_f = 13.4$, $Sc_f = 100 Pr_f$, $\kappa^2 = 9.705\,432$, $T_0^* = 4\,^\circ$C, and $T_u^* = 0\,^\circ$C. In order to compare our results with those of Ref. [11], Fig. 3 displays the stability curves in the plane (R, R_c), with T_b^* varying as shown on graph (i.e., $\xi \in [-3.5, -3.1]$). We note that in our notation, $R = Gr_T^* Pr_f$ and $R_c = Gr_S Sc_f$. The results are in very good agreement with the ones presented on Fig. 1 of Ref. [11]. The kink in the curves represents the point at which convection switches from steady convection ($\sigma_r = \sigma_i = 0$) to oscillatory convection ($\sigma_r = 0$, $\sigma_i \neq 0$).

B. Three-layer system

1. *Physical properties and problem configuration*

Let us now turn our attention to the three-layer system. According to Bogorodskii and Nagurnyi [10], typical values of ice permeability lie in the range 10^{-10}–10^{-6} m^2. On the basis of a series of measurements of ice permeability made in the North American Arctic between 1998 and 2001, Eicken *et al.* [19] derived a relation between the brine volume fraction

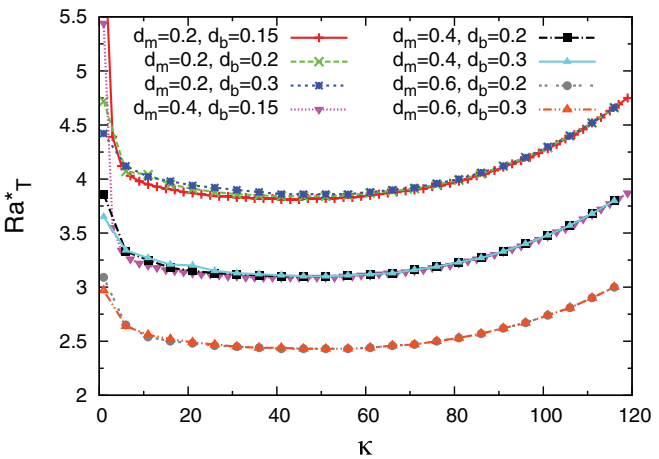

FIG. 6. (Color online) Marginal stability curves for different values of d_m and d_b, and fixed $Ra_S = 900$, $\xi = -1$, and $Da = 10^{-8}$.

TABLE I. Critical Rayleigh number $\mathrm{Ra}^*_{\mathrm{Tcr}}$ for various d_m and d_b. Results obtained for fixed $\mathrm{Ra_S} = 900$.

d_m	$d_m = 0.2$								$d_m = 0.4$			$d_m = 0.6$	
d_b	0.7	0.6	0.5	0.4	0.3	0.2	0.15	0.1	0.3	0.2	0.15	0.3	0.2
$\mathrm{Ra}^*_{\mathrm{Tcr}}$	3.85	3.85	3.85	3.85	3.86	3.84	3.81	3.81	3.1	3.1	3.09	2.43	2.43

ϕ and the ice permeability K:

$$K = 3.738 \times 10^{-11} \exp[7.265\phi]\ \mathrm{m}^2 \quad \text{for} \quad \phi > 0.096. \quad (12)$$

We retain an average value of $K = 10^{-8}$ m^2 (i.e., $\mathrm{Da} = 10^{-8}$, as the vertical extent of the ice pond is $O(1\ \mathrm{m})$ [3]) to obtain from the above relation the approximate value $\phi = 0.77$. Furthermore, the fluid Prandtl number is fixed at $\mathrm{Pr_f} = 13.4$, which is consistent with water at low temperatures. Finally, we take $\mathrm{Le} = \mathrm{Sc_f}/\mathrm{Pr_f} = 100$ and $\varepsilon_T = \alpha_{Tf}/\alpha_{Tm} = 0.3$ [20,21]. The values of Da, ϕ, $\mathrm{Pr_f}$, Le, and ε_T are kept fixed throughout all

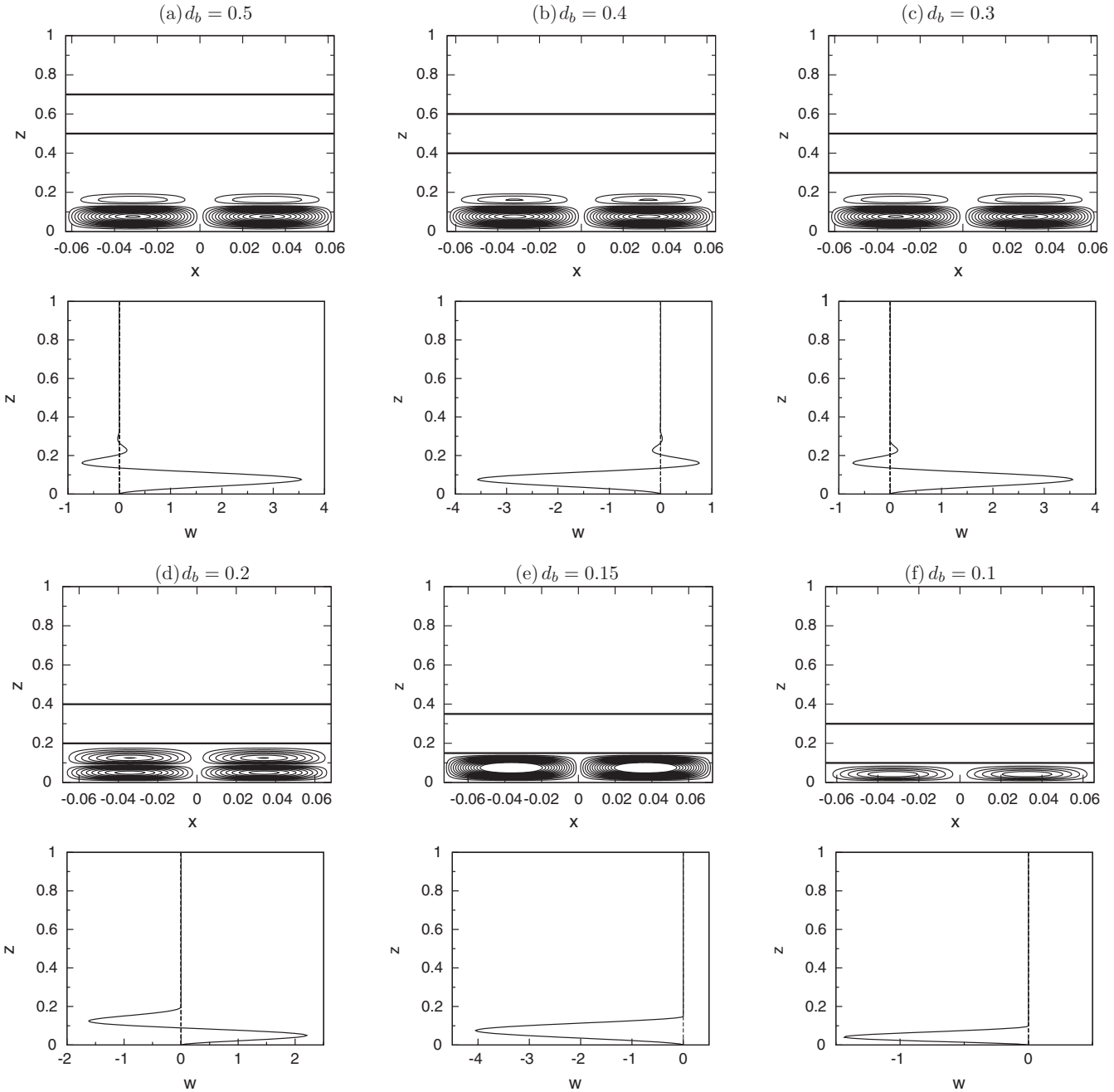

FIG. 7. Streamline patterns ($\Psi_{\max} = \pm 0.07$, $\Delta\Psi = 0.01$) and vertical velocity profiles at the onset of convection for $\mathrm{Ra_S} = 900$, $\xi = -1$, $\mathrm{Da} = 10^{-8}$, $d_m = 0.2$, and different values of d_b. The thick horizontal lines represent the fluid-porous interfaces.

calculations, unless otherwise specified. Results are typically presented in the (Ra_T^*,Ra_S) plane, where the thermal and the solutal Rayleigh numbers are defined by $\mathrm{Ra}_\mathrm{T}^* = \mathrm{Gr}_\mathrm{T}^*\mathrm{Pr}_\mathrm{f}\mathrm{Da}$ and $\mathrm{Ra}_\mathrm{S} = \mathrm{Gr}_\mathrm{S}\mathrm{Sc}_\mathrm{f}\mathrm{Da}$, respectively.

Differently from convection problems concerned with fluids having a linear relation between density and temperature, convection in cold water behaves in a complicated manner. Due to the density maximum several configurations of the base conductive state are possible as follows.

(i) $T_0^* < T_u^*$ [*Fig. 4(a)*]. In this case, two regions can be identified in terms of stability. For $T^* < T_0^*$, density increases with temperature and therefore the temperature gradient is destabilizing; On the contrary, for $T^* > T_0^*$, density decreases with increasing temperature, and the temperature gradient becomes stabilizing as one moves toward the upper part of the system.

(ii) $T_0^* \geqslant T_u^*$ [*Figs. 4(b) and 4(c)*]. Here, the density maximum is located outside of the layer. This means that inside the system we always have $T^* < T_0^*$, corresponding to a destabilizing temperature gradient. In this situation, the "effective"temperature range for the onset of convection is the reference temperature difference ΔT.

Figure 4(a) illustrates a particular situation where the base conductive state is characterized by two superposed regions. The convective movement in the unstable lower region can penetrate into the upper region and destabilize the whole system. The term "penetrative convection"refers to this situation, i.e., systems where one part of the layer has a tendency to become unstable while the rest of the layer tends to remain stable. The convective motion triggered by the instability can affect the stable part of the layer by viscous entrainment and induce a secondary motion. Such penetrative convection systems are usually sensitive to finite amplitude disturbances, revealing the possibility of convective motion below the threshold established by a linear stability analysis. This type of behavior corresponds to subcritical bifurcations and has been observed by Moore and Weiss [22] for a single fluid layer and by Mamou *et al.* [23] for an isotropic porous medium. In the Arctic, the air temperature undergoes seasonal variations, and can achieve 4 °C during summer. Therefore, in the present study we consider $T_u^* \leqslant 4\,^\circ\mathrm{C}$ (or $\xi \leqslant -1$). In this configuration, the whole system is unstable at the base conductive state and thus penetrative convection does not occur. Hence results presented in this section exclusively concern the situations illustrated in Figs. 4(b) and 4(c).

Finally, it is worth recalling that binary fluids subjected to vertical temperature and concentration gradients experience both thermal and solutal stratification. Due to the fact that the fluid density depends on the solute concentration, it leads to a competition between thermal and compositional gradients. This competition between heat and solute diffusion may lead to flow oscillations in the fluid. For the range of parameters studied in this section, a shift from stationary to oscillatory convection is observed for $\mathrm{Ra}_\mathrm{S} \neq 0$.

In the next two sections, we shall focus our attention on the geometrical parameters of the three-layer system: the thickness of the bottom fluid layer ($d_b = d_b^*/d^*$) and the thickness of the porous layer ($d_m = d_m^*/d^*$). In order to study the influence of d_m and d_b, in Secs. IV B2 and IV B3 the following parameters are kept fixed: $\mathrm{Ra}_\mathrm{S} = 900$, $\mathrm{Da} = 10^{-8}$, $\xi = -1$, $\phi = 0.77$, and $\varepsilon_T = 0.3$.

2. *Influence of the thickness of the porous layer*

It is important to remark that there is no symmetry in this problem first because the diffusivity ratios ε_T and ε_S are not equal and moreover due to the quadratic variation of density with respect to temperature. Hence, differently from Ref. [10], even if the porous layer is placed at the midplane of the system, the upper and lower fluid layers do not lose stability simultaneously, i.e., at the same Rayleigh number. For the range of parameters studied in the present work, it has been observed that the onset of convective motion always takes place in the bottom fluid layer, as illustrated in Figs. 5(a)–5(c). This is to be expected since, at the pure conduction state, density gradients are stronger in the lower part of the system [see Figs. 4(b) and 4(c)]. From the vertical velocity profiles it can be noted that there is almost no penetration of the incipient convective flow in the porous matrix. Moreover, it has been observed that the isotherms and the isoconcentration lines at the onset of convection ($\mathrm{Ra}_\mathrm{T}^* = \mathrm{Ra}_\mathrm{Tcr}^*$) are not distorted, a behavior which could characterize a subcritical bifurcation.

The marginal stability curves for three different values of d_m and various d_b are presented in Fig. 6. It can be observed that, for a fixed d_b, the increase of d_m destabilizes the system. The interpretation for this may be given in terms of the characteristics of the bottom fluid layer (thickness d_b and effective temperature and salinity differences in this layer). A simple calculation of the diffusive profiles gives the temperature and salinity at the interface between the porous layer and the bottom fluid layer (T_{mb} and S_{mb}):

$$T_{mb} - T_b = \frac{(T_u - T_b)d_b}{[1 + d_m(\varepsilon_T - 1)]}, \tag{13}$$

$$S_b - S_{mb} = \frac{(S_b - S_u)d_b}{[1 + d_m(\varepsilon_S - 1)]}. \tag{14}$$

For a fixed value of d_b, increasing d_m modifies the temperature and salinity at the interface between the porous medium and the bottom fluid layer depending on the relative values of the diffusivities in the layers (ε_T and ε_S). With $\varepsilon_T = \alpha_{Tf}/\alpha_{Tm} =$

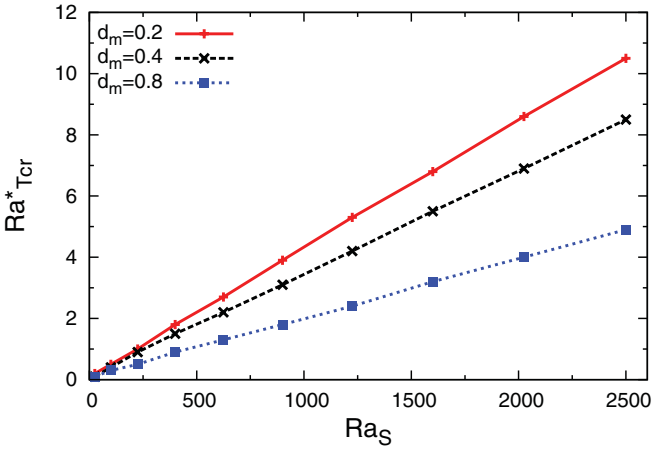

FIG. 8. (Color online) Influence of the thickness of the porous layer (which is placed at the center of the cavity in the three cases presented).

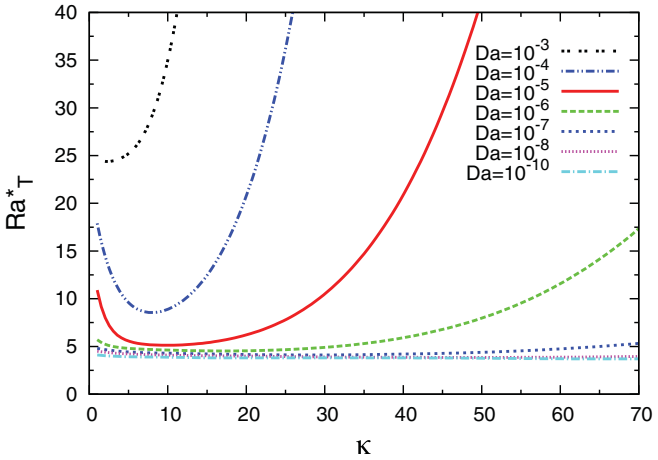

FIG. 9. (Color online) Marginal stability curves obtained for $d_m = 0.2$, $d_b = 0.4$, and different values of the Darcy number.

0.3, increasing d_m increases the interface temperature, and the subsequent larger effective temperature difference makes the layer more unstable. Similarly, as $\varepsilon_S = 1/\phi$ is larger than 1, the salinity difference decreases with increasing d_m and thus the stabilizing solutal effect is smaller. Both mechanisms (increase in the temperature difference and decrease in the salinity difference) are destabilizing and, as a consequence, the marginal stability curves shift down.

3. *Influence of the thickness of the bottom fluid layer*

Table I presents the numerical values of $\mathrm{Ra}^*_{\mathrm{Tcr}}$ corresponding to the three different values of d_m (minima of the curves in Fig. 6). Note that the critical Rayleigh number for the onset of convection remains practically unchanged for varying d_b and fixed d_m. This suggests that the geometrical parameter governing the stability threshold is the depth of the porous layer and that the depths of the fluid layers play a marginal role. As in the previous section, we focus our attention on the characteristics of the bottom fluid layer (where the onset of convection takes place). For a fixed value of d_m, increasing d_b leads to larger temperature and salinity differences in the bottom layer. Thus both the stabilizing solutal effect and the destabilizing thermal effect increase and these two opposing mechanisms tend to compensate each other: our results show that $\mathrm{Ra}^*_{\mathrm{Tcr}}$ remains constant. A possible interpretation for this remarkable feature is that at the bottom fluid layer the density variation with temperature is larger and linear. The ratio of the driving forces $\frac{\beta_S(S_b - S_{mb})}{\beta_T(T_{mb} - T_b)}$ is then independent of d_b.

The streamline patterns and vertical velocity profiles for $d_m = 0.2$ and different values of d_b are presented in Fig. 7. All the cases present almost the same $\mathrm{Ra}^*_{\mathrm{Tcr}}$. However, the flow structure at the onset of convection may be somewhat different: due to the very flat minimum of the marginal stability curves, the same critical Rayleigh number may correspond to different wave numbers. Furthermore, a slight decrease in $\mathrm{Ra}^*_{\mathrm{Tcr}}$ is observed at very small values of d_b [see Figs. 7(e), 7(f), and Table I], due the confinement of the convection cell.

4. *Influence of the physical parameters*

In this section, the influence of the main physical parameters ($\mathrm{Ra_S}$, Da, ξ, ε_T, ε_S) governing the stability of the three-layer system is discussed.

The influence of the imposed salinity gradient is emphasized in Fig. 8, where the stability thresholds are presented in the ($\mathrm{Ra_S}$, $\mathrm{Ra}^*_{\mathrm{Tcr}}$) plane, for $\xi = -1$ and varying d_m and d_b. The porous layer is placed at the middle plan of the cavity in the three cases presented. For the range of parameters studied, the dependence of $\mathrm{Ra}^*_{\mathrm{Tcr}}$ on $\mathrm{Ra_S}$ is somewhat linear. As expected, when the stabilizing salinity gradient becomes more

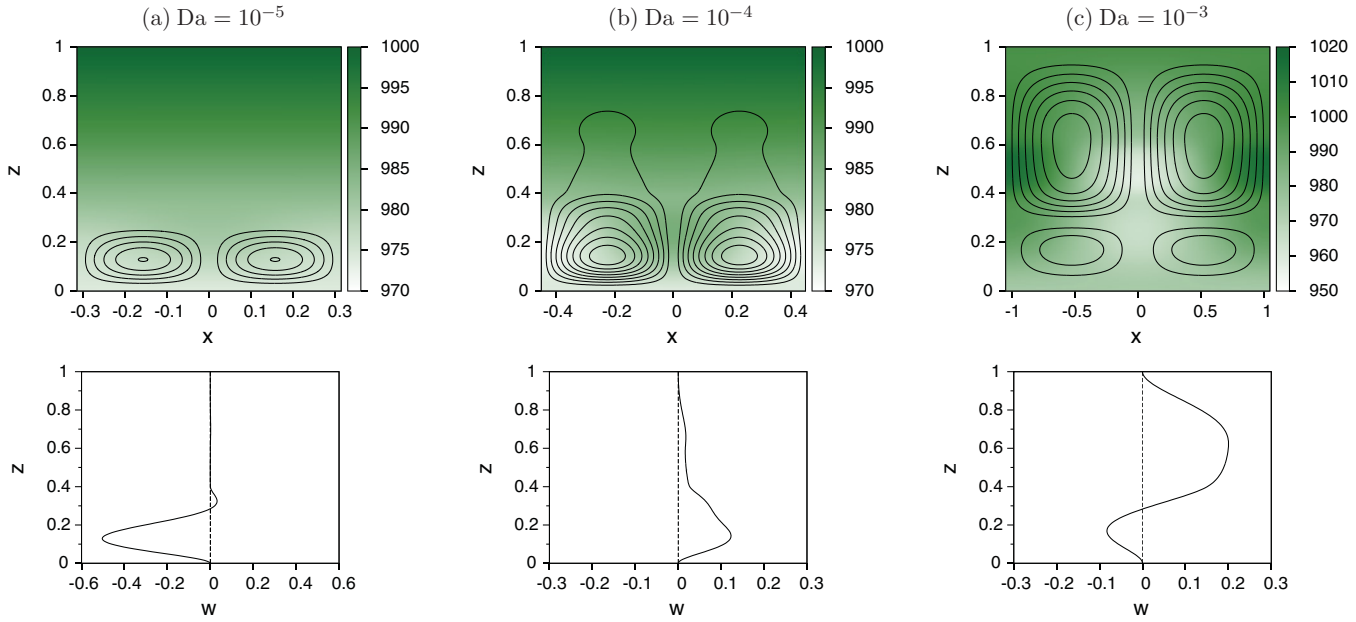

FIG. 10. (Color online) Streamline patterns, density distributions, and vertical velocity profile at the onset of convection for fixed for $d_m = 0.2$, $d_b = 0.4$, and different values of the Darcy number: (a) $\mathrm{Da} = 10^{-5}$ ($\Psi_{\max} = \pm 0.05$, $\Delta\Psi = 0.01$), (b) $\mathrm{Da} = 10^{-4}$ ($\Psi_{\max} = \pm 0.016$, $\Delta\Psi = 0.002$), and (c) $\mathrm{Da} = 10^{-3}$ ($\Psi_{\max} = \pm 0.06$, $\Delta\Psi = 0.01$).

important, a higher Ra^*_{Tcr} is necessary to destabilize the system. However, note that a significant variation of Ra_S implies a very small change in Ra^*_{Tcr}, behavior that characterizes the Hopf bifurcation [24] (see also the fluid layer case presented in Fig. 3). Finally, it can be observed that as the porous layer thickness increases, the stability curves shift down, i.e., the system becomes more unstable. This result confirms the previous findings that instabilities are favored with the increase of d_m, i.e., in larger ice layers.

In order to illustrate the influence of the Darcy number alone, we investigate the hypothetical situation where $\phi = 0.77$ is kept fixed and Da varies. The marginal stability curves of Fig. 9 illustrate the stabilizing character of the Darcy number. For very low values of Da the porous medium behaves as a solid, and for $Da < 10^{-10}$ the stability curves are almost superposed. With the increase of the Darcy number, the penetration of the flow into the porous matrix becomes easier, as shown by the streamlines of Figs. 10: (a) for $Da = 10^{-5}$, the cells are mainly confined in the lower fluid layer; (b) on the contrary, for $Da = 10^{-4}$, the convective movement is characterized by large cells which penetrate into the porous medium and attain the upper fluid layer; (c) finally, for $Da = 10^{-3}$, superposed contrarotating cells which occupy the whole system are observed.

According to Martin and Kauffman [3], the sea water at the bottom of the pond is usually near its freezing point. Assuming that $-1.9\,^\circ\mathrm{C} \leqslant T^*_b \leqslant -1.6\,^\circ\mathrm{C}$ and $0\,^\circ\mathrm{C} \leqslant T^*_u \leqslant 4\,^\circ\mathrm{C}$, we restrict our attention to $\xi \in [-3,-1]$. As mentioned before, in our range of parameters ($T^*_0 \geqslant T^*_u > T^*_b$, i.e., $\xi \leqslant -1$) penetrative convection does not occur. Therefore, the thermal Rayleigh number Ra^*_T has been defined in terms of the pertinent temperature difference for this problem: $\Delta T = T^*_u - T^*_b$. It is nevertheless clear that problems involving a quadratic density profile require the definition of an extra thermal parameter, which accounts for the relative position of the density maximum: $\xi = (T^*_b - T^*_0)/\Delta T$. We note that Ra^*_T and ξ are not independent parameters. For fixed Ra^*_S, $Ra^*_T \propto 1/\xi^2$. In order to establish how ξ affects the stability of the system, we define a modified Rayleigh number $Ra^{**}_{Tcr} = Ra^*_{Tcr}\,\xi^2$ based on $(T^*_b - T^*_0)^2$ instead of $(T^*_u - T^*_b)^2$. In this way, instead

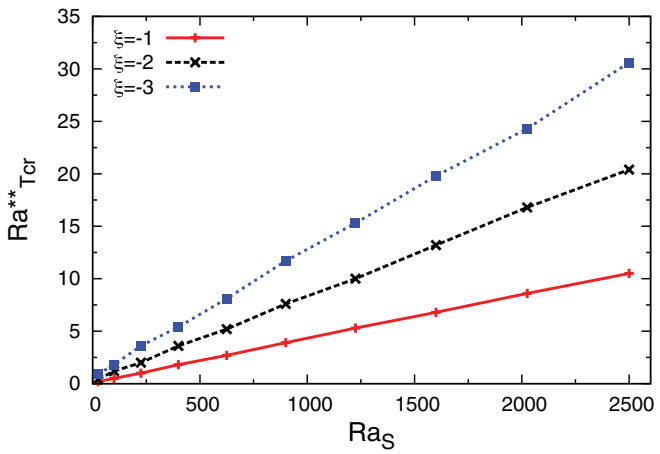

FIG. 11. (Color online) Linear stability thresholds in terms of the modified Rayleigh number $Ra^{**}_{Tcr} = Ra^*_{Tcr}\,\xi^2$ for $d_m = 0.2$, $d_b = 0.4$, and different values of the thermal parameter ξ.

TABLE II. Influence of the thermal and solute diffusivity ratios on the critical Rayleigh number Ra^*_{Tcr}. Results obtained for fixed $Ra_S = 900$.

d_m	$d_m = 0.2$			$d_m = 0.6$		
d_b	0.7	0.7	0.3	0.3	0.3	0.3
ε_T	0.3	1	0.3	1	1	1
ε_S	$(0.77)^{-1}$	$(0.77)^{-1}$	$(0.77)^{-1}$	$(0.77)^{-1}$	1	1
Ra^*_{Tcr}	3.85	4.44	3.86	4.44	4.68	4.68

of $Ra^*_{Tcr} = \mathcal{F}(T^*_u, T^*_b)$ and $\xi = \mathcal{G}(T^*_u, T^*_b)$, we have $Ra^{**}_{Tcr} = \mathcal{H}(T^*_b)$ and $\xi = \mathcal{G}(T^*_u, T^*_b)$. These last two parameters can be varied independently. The stability thresholds for different values of ξ and fixed $d_b = 0.4$, $d_m = 0.2$ are presented in Fig. 11. The inspection of this figure shows that as ξ increases (i.e., for a fixed T^*_b, T^*_u increases), the system becomes more unstable. This is to be expected since the temperature gradient is destabilizing.

Two other important parameters are the ratios of the thermal and mass diffusivities of the fluid and the porous medium. The previous calculations have been made considering that the conductivity of the porous medium is larger than the one of the fluid ($\varepsilon_T = 0.3$) and that the porosity of the porous medium is $\phi = 0.77$, thus $\varepsilon_S = (0.77)^{-1}$.

Results presented in Table II confirm the conclusions that can be drawn from the analysis of expressions (13) and (14). Increasing ε_T from 0.3 to 1 results in a smaller temperature difference in the bottom fluid layer, thus the destabilizing thermal effect is weaker and the instability threshold is larger. ε_S plays an opposite role. It can also be seen in Table II that, for the physically unrealistic situation ($\phi = 1$) where $\varepsilon_T = \varepsilon_S = 1$, the critical temperature and salinity differences, and thus the critical Rayleigh number, do not depend on d_m.

V. CONCLUSIONS AND PERSPECTIVES

A linear stability analysis has been carried out in order to investigate the conditions for the onset of thermosolutal natural convection in under ice melt-ponds. Water density inversion in the neighborhood of 4 °C was taken into account by using a density profile with quadratic temperature dependence and linear concentration dependence. The study of the three-layer system (melt pond–ice matrix–under ice melt-pond) has been performed by considering an isotropic and saturated porous layer sandwiched between two layers of fluid. The system was modeled using a one-domain approach, and the GITT method was used to solve the resulting eigenvalue problem. It has been shown that, under realistic conditions, the onset of convective motion always takes place at the bottom fluid layer and is characterized by oscillatory convective cells. The main geometrical parameter influencing stability is the depth of the ice matrix, while the depths of the upper and lower fluid layers play a marginal role. Systems with larger ice layers are more unstable. Convection is also favored by larger temperature gradients, which is more likely to happen during Arctic summer.

The results presented in this work were obtained for rigid external boundaries. As these boundaries represent the interfaces air–melt water and melt water–sea water, we intend

to extend the analysis by using more realistic boundary conditions. An extension to the nonlinear regime is also foreseeing. Moreover, the investigation of the evolution of false bottoms through direct numerical simulations is underway.

APPENDIX A: BASE STATE

The basic state for the temperature field in the upper fluid layer ($\overline{T}_{fu}$), the porous layer ($\overline{T}_m$), and the bottom fluid layer ($\overline{T}_{fb}$) are, respectively,

$$\overline{T}_u(z) = c_1 z + c_2, \tag{A1}$$

$$\overline{T}_m(z) = c_3 \varepsilon_T z + c_4, \tag{A2}$$

$$\overline{T}_b = c_5 z + c_6, \tag{A3}$$

where

$$c_1 = c_3 = c_5 = \frac{1}{1 + d_m(\varepsilon_T - 1)}, \tag{A4}$$

$$c_2 = \xi + \frac{d_m(\varepsilon_T - 1)}{1 + d_m(\varepsilon_T - 1)}, \tag{A5}$$

$$c_4 = \xi + \frac{d_b(1 - \varepsilon_T)}{1 + d_m(\varepsilon_T - 1)}, \tag{A6}$$

$$c_6 = \xi. \tag{A7}$$

Similarly, the basic state for the concentration field takes the form

$$\overline{S}_{fu}(z) = c_7 z + c_8, \tag{A8}$$

$$\overline{S}_m(z) = \frac{c_9}{\phi} z + c_{10}, \tag{A9}$$

$$\overline{S}_{fb}(z) = c_{11} z + c_{12}, \tag{A10}$$

where

$$c_7 = c_9 = c_{11} = \frac{\phi}{\phi + d_m(1 - \phi)}, \tag{A11}$$

$$c_8 = \frac{d_m(1 - \phi)}{\phi + d_m(1 - \phi)} - \frac{(S_0^* - S_b^*)}{\Delta S}, \tag{A12}$$

$$c_{10} = -\frac{d_b(1 - \phi)}{\phi + d_m(1 - \phi)} - \frac{(S_0^* - S_b^*)}{\Delta S}, \tag{A13}$$

$$c_{12} = \frac{S_b^* - S_0^*}{\Delta S}. \tag{A14}$$

We remark that constants c_8, c_{10}, and c_{12} do not interfere in the analysis.

APPENDIX B: GITT

Following the GITT procedure, we choose the same auxiliary problems (for the velocity, temperature, and concentration fields) as those of Ref. [13]. After applying the integral transformation procedure, the momentum equation takes the form

$$\begin{aligned} &-\sigma \sum_{j=1}^{N_W} \mathcal{M}_{ji} \overline{W}_j + \sum_{j=1}^{N_W} \mathcal{S}_{ji} \overline{W}_j - \kappa^2 \sum_{j=1}^{N_W} \mathcal{F}_{ji} \overline{W}_j \\ &- \sum_{j=1}^{N_W} \mathcal{J}_{ji} \overline{W}_j - \kappa^2 \mathrm{Gr_T} \Delta T \sum_{h=1}^{N_\theta} \mathcal{G}_{hi} \overline{\theta}_h \\ &-\kappa^2 \mathrm{Gr_S} \sum_{l=1}^{N_S} \mathcal{H}_{li} \overline{\mathcal{S}}_l = 0, \quad i = 1, \ldots, N_W, \end{aligned} \tag{B1}$$

where

$$\begin{aligned} \mathcal{M}_{ji} = &- \int_0^1 \left(\frac{1}{\phi} \frac{d^2 \widetilde{\psi}_{W,j}(z)}{dz^2} \right) \widetilde{\psi}_{W,i}(z) dz + \kappa^2 \int_0^1 \frac{1}{\phi}\, \widetilde{\psi}_{W,j}(z) \widetilde{\psi}_{W,i}(z) dz + \left(\frac{1}{\phi} - 1 \right) \left(- \frac{d\widetilde{\psi}_{W,j}(z)}{dz} \frac{d\widetilde{\psi}_{W,i}(z)}{dz} \right) \Bigg|_{z=d_b} \\ &+ \left(\frac{1}{\phi} - 1 \right) \left(\frac{d\widetilde{\psi}_{W,j}(z)}{dz} \frac{d\widetilde{\psi}_{W,i}(z)}{dz} \right) \Bigg|_{z=d_b+d_m}, \end{aligned} \tag{B2}$$

$$\mathcal{S}_{ji} = \int_0^1 \frac{1}{\phi} \left(\mu_i^4 + \kappa^4 \right) \widetilde{\psi}_{W,j}(z) \widetilde{\psi}_{W,i}(z) dz, \tag{B3}$$

$$\begin{aligned} \mathcal{F}_{ji} = &\int_0^1 \left(2 \frac{1}{\phi} \frac{d^2 \widetilde{\psi}_{W,j}(z)}{dz^2} - \frac{1}{\mathrm{Da}} \widetilde{\psi}_{W,j}(z) \right) \widetilde{\psi}_{W,i}(z) dz + 2 \left(1 - \frac{1}{\phi} \right) \left(- \frac{d\widetilde{\psi}_{W,j}(z)}{dz}\, \widetilde{\psi}_{W,i}(z) \right) \Bigg|_{z=d_b} \\ &+ 2 \left(1 - \frac{1}{\phi} \right) \left(\frac{d\widetilde{\psi}_{W,j}(z)}{dz}\, \widetilde{\psi}_{W,i}(z) \right) \Bigg|_{z=d_b+d_m}, \end{aligned} \tag{B4}$$

$$\begin{aligned} \mathcal{J}_{ji} = &\int_0^1 \left(\frac{1}{\mathrm{Da}} \frac{d^2 \widetilde{\psi}_{W,j}(z)}{dz^2} \right) \widetilde{\psi}_{W,i}(z) dz + \left(1 - \frac{1}{\phi} \right) \left(- \frac{d^2 \widetilde{\psi}_{W,j}(z)}{dz^2} \frac{d\widetilde{\psi}_{W,i}(z)}{dz} \right) \Bigg|_{z=d_b} + \left(1 - \frac{1}{\phi} \right) \left(\frac{d^2 \widetilde{\psi}_{W,j}(z)}{dz^2} \frac{d\widetilde{\psi}_{W,i}(z)}{dz} \right) \Bigg|_{z=d_b+d_m} \\ &- \left(1 - \frac{1}{\phi} \right) \left(- \frac{d^3 \widetilde{\psi}_{W,j}(z)}{dz^3}\, \widetilde{\psi}_{W,i}(z) \right) \Bigg|_{z=d_b} - \left(1 - \frac{1}{\phi} \right) \left(\frac{d^3 \widetilde{\psi}_{W,j}(z)}{dz^3}\, \widetilde{\psi}_{W,i}(z) \right) \Bigg|_{z=d_b+d_m} \\ &- \frac{1}{\mathrm{Da}} \left(- \frac{d\widetilde{\psi}_{W,j}(z)}{dz} \widetilde{\psi}_{W,i}(z) \right) \Bigg|_{z=d_b} - \frac{1}{\mathrm{Da}} \left(\frac{d\widetilde{\psi}_{W,j}(z)}{dz} \widetilde{\psi}_{W,i}(z) \right) \Bigg|_{z=d_b+d_m}, \end{aligned} \tag{B5}$$

$$\mathcal{G}_{hi} = \int_0^1 2\overline{T}\, \widetilde{\psi}_{\theta,h}(z) \widetilde{\psi}_{W,i}(z) dz, \tag{B6}$$

$$\mathcal{H}_{li} = \int_0^1 \widetilde{\psi}_{S,l}(z)\widetilde{\psi}_{W,i}(z)dz. \tag{B7}$$

In the expression of $\mathcal{S}_{ji}$, note that μ_i represents the eigenvalue of the auxiliary problem chosen for the velocity field.

The transformed energy equation takes the form

$$-\mathrm{Pr_f}\sigma \sum_{h=1}^{N_\theta} \mathcal{N}_{hn}\overline{\theta}_n - \mathrm{Pr_f} \sum_{j=1}^{N_W} \mathcal{C}_{jn}\overline{W}_j - \left(\beta_n^2 + \kappa^2\right)\overline{\theta}_n + \sum_{h=1}^{N_\theta} \mathcal{L}_{hn}\overline{\theta}_n = 0, \quad n = 1, \ldots, N_\theta, \tag{B8}$$

where

$$\mathcal{N}_{hn} = \int_0^1 \frac{\alpha_{Tf}}{\alpha_T}\widetilde{\psi}_{\theta,h}(z)\widetilde{\psi}_{\theta,n}(z)dz, \tag{B9}$$

$$\mathcal{C}_{jn} = \int_0^1 \frac{\alpha_{Tf}}{\alpha_T}\frac{d\overline{T}}{dz}\,\widetilde{\psi}_{W,j}(z)\widetilde{\psi}_{\theta,n}(z)dz, \tag{B10}$$

$$\mathcal{L}_{hn} = \frac{\alpha_{Tf}-\alpha_{Tm}}{\alpha_{Tm}}\left(-\frac{d\widetilde{\psi}_{\theta,h}(z)}{dz}\,\widetilde{\psi}_{\theta,n}(z)\right)\Big|_{z=d_b} + \frac{\alpha_{Tf}-\alpha_{Tm}}{\alpha_{Tm}}\left(\frac{d\widetilde{\psi}_{\theta,h}(z)}{dz}\,\widetilde{\psi}_{\theta,n}(z)\right)\Big|_{z=d_b+d_m}, \tag{B11}$$

and β_n is the eigenvalue of the auxiliary problem for the temperature field.

Similarly, the transformed concentration equation takes the form

$$-\mathrm{Sc_f}\,\sigma \sum_{l=1}^{N_S} \mathcal{O}_{lk}\overline{\mathcal{S}}_l - \mathrm{Sc_f} \sum_{j=1}^{N_W} \mathcal{E}_{jk}\overline{W}_j - \left(\lambda_l^2 + \kappa^2\right)\overline{\mathcal{S}}_l + \sum_{l=1}^{N_S} \mathcal{D}_{lk}\overline{\mathcal{S}}_l = 0, \quad k = 1, \ldots, N_S, \tag{B12}$$

where

$$\mathcal{O}_{lk} = \int_0^1 \phi\,\widetilde{\psi}_{S,l}(z)\widetilde{\psi}_{S,k}(z)dz, \tag{B13}$$

$$\mathcal{E}_{jk} = \int_0^1 \frac{1}{\phi}\frac{d\overline{\mathcal{S}}}{dz}\,\widetilde{\psi}_{W,j}(z)\widetilde{\psi}_{S,k}(z)dz, \tag{B14}$$

$$\mathcal{D}_{lk} = \frac{1-\phi}{\phi}\left(-\frac{d\widetilde{\psi}_{S,l}(z)}{dz}\widetilde{\psi}_{S,k}(z)\right)\Big|_{z=d_b} + \frac{1-\phi}{\phi}\left(\frac{d\widetilde{\psi}_{S,l}(z)}{dz}\widetilde{\psi}_{S,k}(z)\right)\Big|_{z=d_b+d_m}, \tag{B15}$$

and λ_l is the eigenvalue of the auxiliary problem for the concentration field.

It is important to observe that in the terms evaluated at the interfaces $z = d_b$ and $z = d_b + d_m$, the effective properties ϕ, Da, and α_T assume the constant values of the porous medium, while inside the integrals $\phi = \phi(z)$, $\mathrm{Da} = \mathrm{Da}(z)$, and $\alpha_T = \alpha_T(z)$.

The system of equations (B1), (B8), and (B12) is a generalized eigenvalue problem for σ, which can be written in the following matrix form: $\mathbf{A} - \sigma\ \mathbf{B} = 0$, where

$$\mathbf{A} = \begin{pmatrix} \mathcal{S}_{ji} - \kappa^2\mathcal{F}_{ji} - \mathcal{J}_{ji} & -\kappa^2\mathrm{Gr_T}\ \Delta T\ \mathcal{G}_{hi} & -\kappa^2\mathrm{Gr_S}\ \mathcal{H}_{li} \\ -\mathrm{Pr_f}\ \mathcal{C}_{jn} & -\left(\beta_n^2 + \kappa^2\right)\delta_{hn} + \mathcal{L}_{hn} & 0 \\ -\mathrm{Sc_f}\ \mathcal{E}_{jk} & 0 & -\left(\lambda_l^2 + \kappa^2\right)\delta_{kl} + \mathcal{D}_{lk} \end{pmatrix}$$

and

$$\mathbf{B} = \begin{pmatrix} \mathcal{M}_{ji} & 0 & 0 \\ 0 & \mathrm{Pr_f}\mathcal{N}_{hn} & 0 \\ 0 & 0 & \mathrm{Sc_f}\ \mathcal{O}_{lk} \end{pmatrix}.$$

A and **B** are square matrices of $N = N_W + N_\theta + N_S$ lines and columns.

[1] P. U. Clark, N. G. Pisias, T. F. Stocker, and A. J. Weaver, Nature (London) **415**, 863 (2002).

[2] N. Untersteiner, J. Geophys. Res. **73**, 1251 (1968).

[3] S. Martin and P. Kauffman, J. Fluid Mech. **64**, 507 (1974).

[4] D. Notz, M. G. McPhee, M. G. Worster, G. A. Maykut, K. H. Schlunzen, and H. Eicken, J. Geophys. Res. **108**, 1 (2003).

[5] D. V. Alexandrov and I. G. Nizovtseva, Int. J. Heat Mass Transf. **51**, 5204 (2008).

[6] F. Nansen, *Farthest North* (Constable, Westminster, England, 1897).
[7] H. Eicken, H. R. Krouse, D. Kadko, and D. K. Perovich, J. Geophys. Res. **107**, 8046 (2002).
[8] P. Wadhams, Nature (London) **333**, 161 (1988).
[9] R. Gradinger, Mar. Ecol. Prog. Ser. **131**, 301 (1996).
[10] P. V. Bogorodskii and A. P. Nagurnyi, Dokllady Earth Sci. **373**(5), 885 (2000).
[11] M. Carr, Cont. Mech. Thermodyn. **15**, 45 (2003).
[12] S. C. Hirata, B. Goyeau, D. Gobin, M. Chandesris, and D. Jamet, Int. J. Heat Mass Transf. **52**, 533 (2009).
[13] S. C. Hirata, B. Goyeau, D. Gobin, and R. M. Cotta, Numer. Heat Transfer, Part B **50**, 409 (2006).
[14] S. C. Hirata, B. Goyeau, D. Gobin, M. Carr, and R. M. Cotta, Int. J. Heat Mass Transf. **50**, 1356 (2007).
[15] S. C. Hirata, B. Goyeau, and D. Gobin, Transp. Porous Media **78**, 525 (2009).
[16] D. Gobin and R. Bennacer, Int. Comm. Heat Mass Transf. **23**, 971 (1996).
[17] S. Whitaker, *The Method of Volume Averaging (Theory and Applications of Transport in Porous Media)* (Springer, New York, 1999).
[18] R. M. Cotta, *Integral Transforms in Computational Heat and Fluid Flow* (CRC Press, Boca Raton, 1993).
[19] H. Eicken, T. C. Grenfell, D. K. Perovich, J. A. Richter-Menge, and K. Frey, J. Geophys. Res. **109**, C08007 (2004).
[20] W. Unterberg, Dept. Eng. UCLA Report No. 64-21, 1964 (unpublished).
[21] B. A. Savel'ev, *Glaciology* (Mosk. Gos. Univ., Moscow, 1991).
[22] D. R. Moore and N. O. Weiss, J. Fluid Mech. **61**, 553 (1973).
[23] M. Mamou, L. Robillard, and P. Vasseur, Int. J. Heat Mass Transf. **42**, 4487 (1999).
[24] D. Nield, J. Fluid Mech. **29**, 545 (1967).